Quantified Design Guidelines of a Compact Transformerless Active EMI Filter for Performance, Stability, and High Voltage Immunity

Dongil Shin, Sangyeong Jeong, and Jingook Kim, *Senior Member, IEEE*

***Abstract*—This paper proposes and analyzes a compact transformerless common mode active electromagnetic interference (EMI) filter (AEF) using a push–pull amplifier. Quantified design guidelines are then rigorously derived from the analysis with consideration for performance, stability, and high voltage transient immunity. The proposed AEF is manufactured based on the design guidelines, and its performance is validated by measurements using a vector network analyzer. The AEF is then implemented into a real 2.2 kW current resonant inverter, and the conducted emissions are reduced by 5–25 dB at a frequency range from 150 kHz to 6 MHz. In addition, the AEF's immunity against high voltage transients is demonstrated by lightning surge tests.**

***Index Terms*—Active EMI filter (AEF), common mode (CM), conducted emission (CE), electromagnetic interference (EMI), high voltage transient, immunity, lighting surge, voltage sense current compensation.**

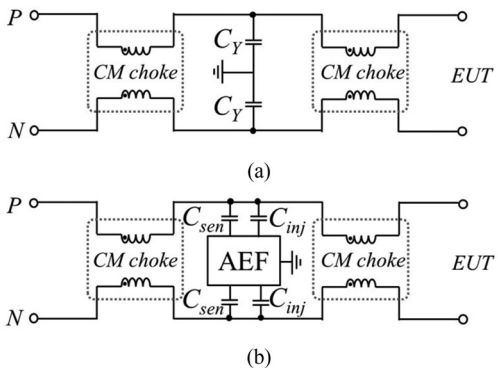

Fig. 1. (a) A typical CM EMI filter with passive *L–C–L* configuration; and (b) the transformerless AEF employed in the filter configuration.

I. Introduction

As a power converting system advances operating at a fast switching frequency, both conducted and radiated emissions become more serious, and the electromagnetic interference (EMI) problems come to be critical issues in the switching mode power supply (SMPS) design [1]–[3]. The electromagnetic compatibility standards such as FCC and CISPR define the limit of conducted and radiated emissions in consumer and industry products. The conducted emissions (CEs) are regulated at relatively low frequencies below 30 MHz, whereas the radiated emissions are at a higher frequency range, from 30 MHz to 1 GHz.

An EMI filter composed of common mode (CM) chokes and Y-capacitors is usually employed on the power input side of an equipment under test (EUT), such as SMPS, to suppress the CM-CEs. The configuration in Fig. 1(a) is one of the typical EMI filters and consists of two CM chokes and a Y-capacitor C_Y, as the *LCL* T-type filter. X-capacitors are also usually employed together to suppress the differential mode (DM)-CEs, but are not shown here in the view of the CM noise. The CM noise currents from the EUT are reduced by the high impedance of CM chokes and the low impedance shunt path due to C_Y. Although the EMI filter can be easily implemented, it has some limitations. A large Y-capacitor may cause dangerous leakage currents exceeding safety regulation limits and is therefore prohibited [3]. To achieve a sufficient CM-conducted noise reduction at the low-frequency range, multiple *LC* stages are thus employed, which occupy a lot of space. Also, in practice, the magnetic flux generated by the ac current partly remains inside the CM choke and magnetically saturates the core of the choke. The CM impedance of the choke can be significantly decreased due to magnetic saturation, and the overall performance of the EMI filter is degraded when employed in a high power system [4]–[6]. An expensive core material is required to avoid such magnetic saturation. Furthermore, thick wire in the CM choke is required for high power applications. Thus, the size and cost of the CM choke remain design issues in EMI filters.

Active EMI filters (AEFs) have been suggested to effectively suppress the CEs [7]–[29]. The topology of AEFs has been outlined in [8], and each topology has been analyzed based on the ideal amplifier model in [9] and [10]. The AEF structures can be divided into the sensing part, amplifier, and compensation parts. The noise captured at the sensing part is converted into the compensation signal by the amplifier, which is then injected through the compensation part to reduce the CEs. The transformers can be utilized to capture the noise current as a sensing component,

Manuscript received April 19, 2017; revised July 7, 2017 and September 2, 2017; accepted October 10, 2017. Date of publication October 15, 2017; date of current version April 20, 2018. This work was supported by the Basic Science Research Program through the National Research Foundation of Korea under Grant NRF-2016R1D1A1B03934382. Recommended for publication by Associate Editor Luca Dalessandro. *(Corresponding author: Jingook Kim.)*

The authors are with the School of Electrical and Computer Engineering, Ulsan National Institute of Science and Technology, Ulsan 44919, South Korea (e-mail: shindongil@unist.ac.kr; jsy9121@unist.ac.kr; jingook@unist.ac.kr).

Digital Object Identifier 10.1109/TPEL.2017.2763972

and/or to compensate the noise voltage at the compensation part. The capacitors are employed to sense the noise voltage at the sensing part and to inject the current at the compensation part. On the other hand, the amplifier part in the AEF can be implemented with either an operational amplifier (OP-amp) or a push–pull amplifier. Any combination of push–pull amplifiers and OP-amps can also be used.

Many types of AEFs employing OP-amps have been proposed in [11]–[16]. The loop gain of the AEF has been extracted to evaluate the stability in [11], and the performances of the AEFs using an OP-amp have been explained through the impedance variation by the AEFs in [13]–[15]. The general modeling method for the AEFs using OP-amps has been proposed in [16]. Designing an AEF using the OP-amps provides a higher degree of freedom in the amplifier design; however, the cost of the OP-amp is higher than a simple push–pull amplifier, and the immunity of the sensitive OP-amp circuits against high voltage transient is difficult to achieve. Since the cost and reliability are critical factors in the house appliance equipment, the AEF using a simple push–pull amplifier is much preferred in those applications.

In [17]–[21], the AEFs based on a push–pull amplifier for the CM noise reduction in the induction motor system and house appliance have been presented. The voltage sense voltage compensation (VSVC) AEF in [17]–[20] captures the CM voltage generated by the motor operation and cancels the CM noise by injecting the compensation signal to the load side. In the VSVC AEF using a push–pull amplifier, the high voltage rating bipolar junction transistors (BJTs) and high supply voltage are required to generate the sufficient amount of compensating voltage signal. The current sense current compensation (CSCC) AEF using the push–pull amplifier with the low voltage rating BJTs has been also developed in [21]. The supply for the CSCC AEF has been provided from the dc power of the control board for the inverter. All of the AEFs in [17]–[21], however, utilize at least a transformer for the noise sense or compensation. When the transformer is employed in an AEF, the performance of the AEF can be degraded predominantly due to the parasitic components and/or magnetic saturation of the transformer.

Another kind of AEFs, which generate compensation signals from the digitally controlled signals, has been also proposed in [22]–[28]. The AEF also utilize the push–pull amplifiers, but the inputs to the amplifiers are digitally synthesized based on the direct knowledge of the switching noise pulses. The compensation signal is injected into the power lines through either a transformer or a capacitor. Although the digital active filter without a transformer can be developed by using only capacitors, the digital control part is much more complicated, expensive, and larger than the analog sensing AEFs.

Finally, the analog AEF using a simple push–pull amplifier without any transformers has been proposed by Shin *et al*. in [29] for the first time. As compared to the VSCC with the OP-amp in [15], the proposed AEF is implemented with much less transistors. The proposed AEF can be manufactured in a smaller size than the AEFs with the transformer in [17]–[21]. Also, differently from the AEFs in [17]–[20], the proposed VSCC AEF can provide a sufficient noise reduction even under a low-level supply voltage, and low-cost BJTs with a low voltage rating can be employed. The low-level supply voltage for the AEF is provided from the dc power of the control board for the main power system. In summary, the novel features of the proposed AEF can be characterized as 1) the push–pull amplifier with the low voltage rating BJTs, 2) transformerless, and 3) direct analog noise sensing.

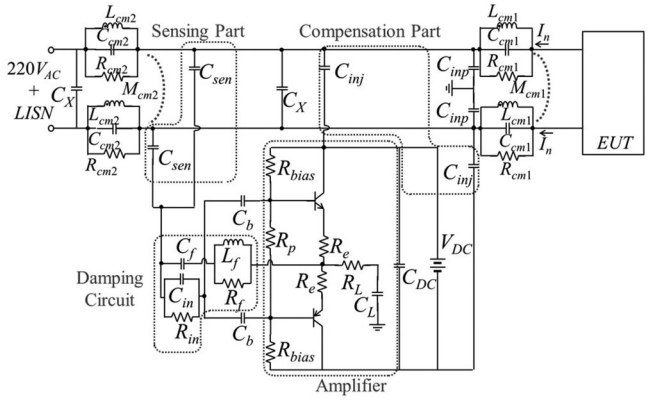

Fig. 2. Schematics of the *L–C–L* EMI filter with the proposed AEF.

The proposed AEF can be used alone, but it would more likely be used together with other filter components. Fig. 1(b) demonstrates a usage example, where the AEF replaces the Y-capacitor of the total filter shown in Fig. 1(a). Although the circuit analysis of the VSCC AEF has been conducted and its loop gain was derived in [29], it cannot be used in the stability analysis of real applications, since other components in the total EMI filter, such as CM chokes, also significantly affect the overall system stability. In addition, to apply the proposed AEF to real industrial and commercial products, the immunity against the high voltage transient should be tested and guaranteed.

This paper completely analyzes the compact transformerless AEF using a push–pull amplifier. Quantified design guidelines are then rigorously derived from the analysis with consideration for performance and stability. For practical applications, the design rules of protection circuits against the high voltage transient are also proposed. Based on the developed design guidelines, the proposed AEF is manufactured and employed in the *L–C–L* EMI filter structure, as shown in Fig. 1(b). The performance of the proposed AEF is validated by measurements using a vector network analyzer (VNA). The AEF is applied to a real 2.2 kW current resonant inverter, and the CEs are reduced by 5–25 dB at the frequency range from 150 kHz to 6 MHz. Also, the immunity of the proposed AEF against high voltage transients is verified by lightning surge tests.

II. Analysis of the Proposed EMI Filter With the AEF

In this section, the EMI filter with the compact transformerless AEF is proposed and completely analyzed.

A. Circuit Model of the Total EMI Filter With the AEF

The complete circuit model of the proposed *L–C–L* EMI filter is shown in Fig. 2, where the AEF plays a role as a Y-capacitor.

For accurate analysis up to several tens of MHz, the CM chokes are modeled as parallel impedances of $L_{\rm cm1}$, $M_{\rm cm1}$, $R_{\rm cm1}$, and $C_{\rm cm1}$ ($L_{\rm cm2}$, $M_{\rm cm2}$, $R_{\rm cm2}$, and $C_{\rm cm2}$), as shown in Fig. 2. They represent the self-inductance, mutual inductance, equivalent parallel resistance, and equivalent parallel capacitance in the CM chokes, respectively. Additional input filter capacitors $C_{\rm inp}$ are located between CM chokes to suppress the effects of the EUT impedance on the AEF operation. Two X-capacitors C_X are also placed to reduce the differential noises from the EUT. I_n represents the CM noise current generated by the EUT. The AEF block can be divided into the sensing part, the injection part, the amplifier, and the damping circuits. The noise voltage is captured by the sensing capacitors $C_{\rm sen}$ and applied to the amplifier input. The compensation currents, which are generated by the amplifier, flow into the power lines through the injection capacitors ($C_{\rm inj}$). The push–pull amplifier in the AEF is designed as a class AB amplifier with the output load of R_L and C_L. A dc source $V_{\rm dc}$ is supplied as the power supply for the amplifier. The ac utility voltage and the noise from the EUT can be coupled to the dc supply of the proposed AEF, which can lead to a bias distortion and malfunction of the AEF. Also, if the AEF supply is provided from a control board inside the application product, it can remove the proper isolation between control and power sections. However, after adding the bulk decoupling capacitor $C_{\rm dc}$ with the value of a few μF, the coupled noise voltage is greatly reduced, and the AEF operates properly. The decoupling capacitor is an essential component in the AEF circuit. The BJTs in the amplifier are biased by the resistors $R_{\rm bias}$ and R_p. The degeneration emitter resistors R_e are also added to stabilize the bias. The dc block capacitors C_b are connected in series between the sensing part and the amplifier input to mitigate the electric overstress that might be caused by large dc voltage differences. The output current of the proposed AEF affects the input voltage, and therefore the AEF is a feedback system. For feedback stability, damping circuit elements are added to the input side of the push–pull amplifier. $R_{\rm in}$ and $C_{\rm in}$ in parallel are located between $C_{\rm sen}$ and C_b. Also, C_f, R_f, and L_f comprise another damping branch from $C_{\rm sen}$ to R_e. The necessity and behavior of the damping circuits will be analyzed in detail in Section IV.

B. Circuit and Block Diagram Analysis

The performance and stability of the EMI filter in Fig. 2 can be accurately investigated using a detail circuit analysis. The loop gain is the most important factor when analyzing a feedback system. In extracting the loop gain, the circuit analysis should be conducted with consideration for all components in the total EMI filter, since all the components affect the system's stability. The expressions of the circuit model are then converted a block diagram, where the loop gain can be effectively extracted.

The proposed AEF is predominantly symmetric regarding the earth ground and can be analyzed by using only half of the circuits. The equivalent circuit model of the half-portion was developed by applying the small signal model of a BJT, as shown in Fig. 3(a). The small signal model of a BJT consists of r_π, C_π, C_μ, and g_m, which correspond to the input resistance, base–emitter capacitance, base–collector capacitance, and transconductance, respectively. I_b, I_x, I_o, I_f, $I_{\rm inp}$, and $I_{\rm LISN}$ represent the base current, the current flowing through $R_{\rm bias}$ and C_μ, the collector current, the current flowing through a damping branch, the current flowing to $C_{\rm inp}$, and the current flowing through the line impedance stabilization network (LISN), respectively. V_π represents the voltage between the base and emitter of the BJT, and $V_{\rm AEF}$ represents the noise voltage at the node where the AEF part is connected. V_B and V_C indicate the node voltages at base and collector, respectively.

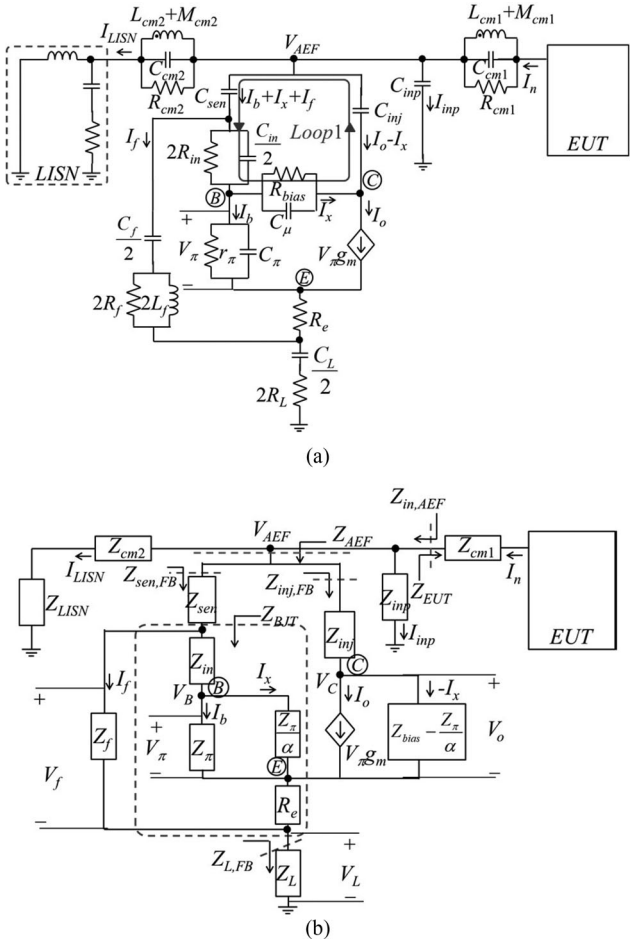

Fig. 3. (a) The equivalent circuit model of the EMI filter with AEF and (b) the circuit model after applying Miller's theorem.

By applying the KVL along *Loop*1 in Fig. 3(a), the ratio of I_x to I_b, which is designated as α, is derived as

$$\frac{I_x}{I_b} = \alpha = \frac{Z_{\rm inj}Z_\pi g_m - Z_{\rm sen} - Z_{\rm in} - \frac{Z_{\rm sen}}{Z_f}\left(Z_{\rm in} + Z_\pi + R_e\left(1 + Z_\pi g_m\right)\right)}{Z_{\rm sen} + Z_{\rm in} + Z_{\rm bias} + Z_{\rm inj} + \frac{Z_{\rm sen}}{Z_f}Z_{\rm in}} \tag{1}$$

where

$$Z_{\rm inj} = \frac{1}{sC_{\rm inj}},\ Z_{\rm sen} = \frac{1}{sC_{\rm sen}},\ Z_\pi = r_\pi \left\| \frac{1}{sC_\pi} \right.,$$
$$Z_{\rm in} = 2R_{\rm in} \left\| \frac{2}{sC_{\rm in}} \right.,\ Z_{\rm bias} = R_{\rm bias} \left\| \frac{1}{sC_\mu} \right. \approx R_{\rm bias},$$
$$Z_f = \frac{2}{sC_f} + 2R_f \,\|2sL_f \ .$$

For simplification, the internal feedback path through $R_{\rm bias}$ and C_μ can be disconnected using parameter α, based on the miller theorem, as shown in Fig. 3(b). That is, the impedance Z_π/α is connected between the base and emitter, while the impedance $Z_{\rm bias} - Z_\pi/\alpha$ is connected between the collector and emitter. Each current and voltage can be expressed as a function of $V_{\rm AEF}$ as

$$I_n = (I_b + I_x + I_f) + (I_o - I_x) + I_{\rm LISN} + I_{\rm inp} \tag{2}$$

$$V_\pi = \frac{Z_f \,\|Z_{\rm BJT}}{Z_{\rm sen,FB}} \frac{Z_\pi \left\| \frac{Z_\pi}{\alpha} \right.}{Z_{\rm BJT}} V_{\rm AEF} \tag{3}$$

$$I_b + I_x = \frac{V_\pi}{Z_\pi \left\| \frac{Z_\pi}{\alpha} \right.} = \frac{Z_f \,\|Z_{\rm BJT}}{Z_{\rm sen,FB} Z_{\rm BJT}} V_{\rm AEF} \tag{4}$$

$$I_o = V_\pi g_m = \frac{Z_f \,\|Z_{\rm BJT}}{Z_{\rm sen,FB}} \frac{Z_\pi \left\| \frac{Z_\pi}{\alpha} \right.}{Z_{\rm BJT}} g_m V_{\rm AEF} \tag{5}$$

$$I_x = \frac{Z_f \,\|Z_{\rm BJT}}{Z_{\rm sen,FB}} \frac{Z_\pi \left\| \frac{Z_\pi}{\alpha} \right.}{Z_{\rm BJT}} \frac{\alpha}{Z_\pi} V_{\rm AEF} \tag{6}$$

$$I_f = \frac{Z_f \,\|Z_{\rm BJT}}{Z_{\rm sen,FB}} \frac{1}{Z_f} V_{\rm AEF} \tag{7}$$

$$I_{\rm inp} + I_{\rm LISN} = \frac{V_{\rm AEF}}{Z_{\rm inp} \| \left(Z_{\rm cm2} + Z_{\rm LISN}\right)} \tag{8}$$

where

$$Z_{\rm inp} = \frac{1}{sC_{\rm inp}}, \tag{9}$$

$$Z_{\rm cm2} = s\left(L_{\rm cm2} + M_{\rm cm2}\right) \left\| \frac{1}{sC_{\rm cm2}} \right\| R_{\rm cm2}, \tag{10}$$

$$Z_{\rm sen,FB} = \frac{V_{\rm AEF}}{I_b - I_x + I_f} = Z_{\rm sen} + Z_f \,\|Z_{\rm BJT} + Z_{L,\rm FB}, \tag{11}$$

$$Z_{\rm inj,FB} = \frac{V_{\rm AEF}}{I_o - I_x} = \frac{Z_{\rm sen,FB}}{\left(\frac{Z_f \,\|Z_{\rm BJT}}{Z_{\rm BJT}}\right)\left(Z_\pi \left\| \frac{Z_\pi}{\alpha} \right.\right)\left(g_m - \frac{\alpha}{Z_\pi}\right)}, \tag{12}$$

$$Z_{\rm BJT} = \frac{V_f}{I_b + I_x} = Z_{\rm in} + Z_\pi \left\| \frac{Z_\pi}{\alpha} \right. + R_e \left(\frac{1 + Z_\pi g_m}{1 + \alpha}\right), \tag{13}$$

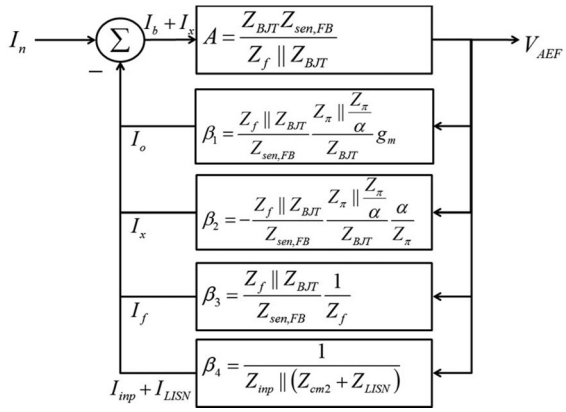

Fig. 4. Block diagram of the EMI filter with the AEF.

$$Z_{L,\rm FB} = \frac{V_L}{I_b + I_x + I_f} = \left(\frac{2}{sC_L} \,\|2R_L\right) \frac{I_b + I_o + I_f}{I_b + I_x + I_f}$$
$$= \left(\frac{2}{sC_L} + 2R_L\right)\left(\frac{1 + Z_\pi g_m}{1 + \alpha} \frac{Z_f \,\|Z_{\rm BJT}}{Z_{\rm BJT}} + \frac{Z_f \,\|Z_{\rm BJT}}{Z_f}\right). \tag{14}$$

To effectively analyze the EMI filter with the AEF, a block diagram can be drawn using the expressions (2)–(8), as depicted in Fig. 4. The feedback type of the proposed EMI filter is the shunt–shunt configuration, since the AEF samples a portion of $V_{\rm AEF}$ as V_π, and converts it to a current [30]. Therefore, the input and output of the block diagram are determined by I_n and $V_{\rm AEF}$. In Fig. 4, A represents the forward transfer function, which is determined by the ratio of $V_{\rm AEF}$ to $(I_b + I_x)$, and β_1 to β_4 correspond to the feedback transfer functions determined by the ratio of each branch current to $V_{\rm AEF}$.

C. Loop Gain and Impedance Analysis

The total closed loop transfer function, which is the ratio of $V_{\rm AEF}$ to I_n, corresponds to the impedance seen at the sensing node to the LISN, indicated as $Z_{\rm in,AEF}$ in Fig. 4(b). Based on the block diagram reduction rules, $Z_{\rm in,AEF}$ and the loop gain of the EMI filter with the proposed AEF can be expressed as

$$Z_{\rm in,AEF} = \frac{V_{\rm AEF}}{I_n} = \frac{A}{1 + A\beta_t} = \frac{1}{\frac{1 + A(\beta_1 + \beta_2 + \beta_3)}{A} + \beta_4}$$
$$= \frac{A}{1 + A\left(\beta_1 + \beta_2 + \beta_3\right)} \left\| \frac{1}{\beta_4} \right.$$
$$= Z_{\rm AEF} \,\|Z_{\rm inp}\| \left(Z_{\rm cm2} + Z_{\rm LISN}\right) \tag{15}$$

where

$$A\beta_t = \left(Z_\pi \left\| \frac{Z_\pi}{\alpha} \right.\right)\left(g_m - \frac{\alpha}{Z_\pi}\right) + \frac{Z_{\rm BJT}}{Z_f} \times \left(1 + \frac{Z_{\rm sen,FB}}{Z_{\rm inp} \| \left(Z_{\rm cm2} + Z_{\rm LISN}\right)}\right) + \frac{Z_{\rm sen,FB}}{Z_n \| \left(Z_{\rm cm2} + Z_{\rm LISN}\right)} \tag{16}$$

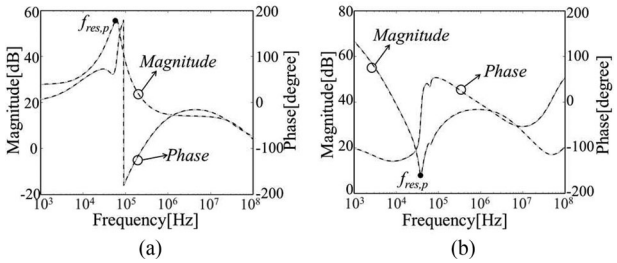

Fig. 5. Calculation (dashed lines) and simulation (solid lines) results: (a) impedance seen at the sensing node to the LISN $Z_{\mathrm{in,AEF}}$ and (b) the loop gain of the EMI filter with AEF $A\beta_t$.

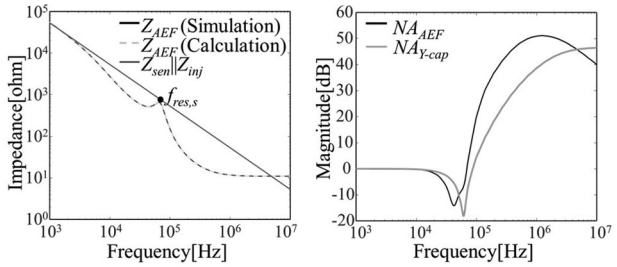

Fig. 6. (a) The impedance of the AEF part Z_{AEF} and (b) NA due to the AEF and passive Y-capacitor.

$$Z_{\mathrm{AEF}} = \frac{V_{\mathrm{AEF}}}{I_b + I_o + I_f} = \frac{A}{1 + A\left(\beta_1 + \beta_2 + \beta_3\right)} = \frac{Z_{\mathrm{sen,FB}}}{1 + \left(\frac{Z_f \| Z_{\mathrm{BJT}}}{Z_{\mathrm{BJT}}}\right)\left(Z_\pi \left\| \frac{Z_\pi}{\alpha}\right.\right)\left(g_m - \frac{\alpha}{Z_\pi}\right)}. \quad (17)$$

β_t is the sum of the feedback transfer functions from β_1 to β_4, and $A\beta_t$ corresponds to the loop gain of the total EMI filter. Z_{AEF} represents the impedance looking at the sensing node in the AEF part, as also indicated in Fig. 3(b). Thus, it is verified from (15) that $Z_{\mathrm{in,AEF}}$ consists of the parallel impedance of Z_{AEF}, Z_{inp}, and $(Z_{\mathrm{cm2}} + Z_{\mathrm{LISN}})$, as it can be expected from the circuit structure. The feedback path by β_4 is related to the parallel impedance of $(Z_{\mathrm{cm2}} + Z_{\mathrm{LISN}})$ and Z_{inp}, whereas the other feedback paths from β_1 to β_3 are involved with Z_{AEF}.

$Z_{\mathrm{in,AEF}}$ and $A\beta_t$ are calculated from (15) and (16) with the given circuit parameter values, and validated by SPICE simulations, as shown in Fig. 5. In Fig. 5(a), the peak of $Z_{\mathrm{in,AEF}}$ occurs due to the *L–C* parallel resonance among Z_{cm2}, Z_{inp}, and Z_{AEF}. The EMI filter might be unstable at the parallel resonance frequency $f_{\mathrm{res},p}$, since the phase of $A\beta_t$ tends to drastically change at $f_{\mathrm{res},p}$, as shown Fig. 5(b). The expressions for $f_{\mathrm{res},p}$ and stability will be further discussed in Section IV.

Z_{AEF} is also calculated from (17) and validated by the SPICE simulation, as shown in Fig. 6(a). Z_{AEF} is compared to the parallel impedance of $(Z_{\mathrm{sen}}||Z_{\mathrm{inj}})$ and shows much lower impedance from 6 kHz to 5 MHz. This means that the effective capacitance between the power lines and the earth ground is greatly increased by the AEF operation. Consequently, a large Y-capacitance is achieved by the AEF in the CEs range, which can greatly attenuate the CM-CEs. However, peak Z_{AEF} occurs due to the series resonance between L_f and C_f in the damping circuit. At the series resonance frequency $f_{\mathrm{res},s}$, the impedance of the damping branch is decreased, resulting in a small base–emitter voltage of the BJT. Accordingly, the AEF's performance can be degraded by the damping circuit, which will be further discussed in Section IV.

Finally, the effect of the AEF on the noise attenuation (NA) of the total EMI filter is investigated. By defining $I_{\mathrm{LISN,w/oAEF}}$ and $I_{\mathrm{LISN,w/AEF}}$ as the LISN current without and with the AEF part, respectively, the NA due to the AEF is calculated as the ratio of $I_{\mathrm{LISN,w/oAEF}}$ to $I_{\mathrm{LISN,w/AEF}}$ as

$$\mathrm{NA_{AEF}} = \frac{I_{\mathrm{LISN,w/oAEF}}}{I_{\mathrm{LISN,w/AEF}}} = \frac{Z_{\mathrm{cm2}} + Z_{\mathrm{LISN}} + Z_{\mathrm{AEF}} \| Z_{\mathrm{inp}}}{Z_{\mathrm{AEF}} \| Z_{\mathrm{inp}}}. \quad (18)$$

The AEF's effectiveness can be verified by comparing it to the EMI filter with passive Y-capacitors in Fig. 1(a), since the AEF plays the role of the Y-capacitors. To make a fair comparison, the value of the passive Y-capacitor C_Y is set as the sum of C_{sen}, C_{inj}, and C_{inp}, which are utilized in the filter with the proposed AEF.

The NA due to the passive Y-capacitor is also calculated as

$$\mathrm{NA}_{Y-\mathrm{cap}} = \frac{I_{\mathrm{LISN,w/o}Y-\mathrm{cap}}}{I_{\mathrm{LISN,w}/Y-\mathrm{cap}}} = \frac{Z_{\mathrm{cm2}} + Z_{\mathrm{LISN}} + Z_{\mathrm{sen}} \| Z_{\mathrm{inj}} \| Z_{\mathrm{inp}}}{Z_{\mathrm{sen}} \| Z_{\mathrm{inj}} \| Z_{\mathrm{inp}}} \quad (19)$$

where $I_{\mathrm{LISN,w/o}_{Y-\mathrm{cap}}}$ and $I_{\mathrm{LISN,w}/Y-\mathrm{cap}}$ represent the LISN current without and with the passive Y-capacitors, respectively.

$\mathrm{NA_{AEF}}$ and $\mathrm{NA}_{Y-\mathrm{cap}}$ have been calculated with the given circuit parameter values and compared in Fig. 6(b). $\mathrm{NA_{AEF}}$ is significantly higher than $\mathrm{NA}_{Y-\mathrm{cap}}$ from 100 kHz to 5 MHz, which is attributed to the smaller impedance of the AEF in Fig. 6(a). That is, the effective capacitance increased by the AEF results in an increase in the NA of CM-CEs.

The effects of the increased capacitance on the safety requirements should also be investigated. The touch or leakage current flowing through a human body is limited by the regulations such as UL101-2002 and IEC60990. Under the "let-go" measurement condition imposing the worst leakage current for the AEF, the measuring network has a low-pass filter characteristic below 1 kHz, and the leakage current is predominantly generated by the low-frequency voltage or currents below 1 kHz [31]. As shown in Fig. 6(a), the proposed AEF increases the effective capacitance between the power lines and the earth ground predominantly in the CEs frequency range above 150 kHz. Since the impedance below 1 kHz is rarely affected by the AEF, the influence of the AEF on the safety requirements for the leakage current is very limited. The AEF can attenuate the CEs without sacrificing the safety, which is the great advantage of using the AEF.

III. Design Guidelines of the Proposed AEF for the Performance

In this section, the design guidelines for optimized performance are derived from an investigation into the AEF impedance $Z_{\rm AEF}$. Although the push–pull amplifier in the proposed AEF is quite simple, the push–pull amplifier should be carefully designed since the bandwidth of a BJT and bias circuit affect the AEF performance.

A. Selection of $C_{\rm inp}$, $C_{\rm sen}$, $C_{\rm inj}$, and $C_{\rm dc}$

The AEF performance is also affected by the impedance looking from the sensing node into the noise source, which is indicated as $Z_{\rm EUT}$ in Fig. 3(b). Its value depends on the CM choke and impedance of the noise source. The impedance of CM noise source is typically related to the parasitic capacitance C_n, among the switching components, heat sink, and earth ground [1]. Since C_n is generally quite small, in tens of pF, the value of $Z_{\rm EUT}$ is predominantly determined by C_n. To eliminate the effect of $Z_{\rm EUT}$ on the AEF performance, the input filter capacitors $C_{\rm inp}$ are used to screen out $Z_{\rm EUT}$. Thus, the value of $C_{\rm inp}$ should be sufficiently larger than C_n. A convenient guideline can be chosen as

$$C_{\rm inp} \geq 5C_n. \tag{20}$$

Expressions (1)–(17) have already neglected the effect of $Z_{\rm EUT}$.

As shown in Fig. 6, the variation of $Z_{\rm AEF}$ is the most responsible for the NA of the AEF, and the main design factors can be extracted from its expression. However, the expression of (17) is too complicated due to the damping circuits. The damping circuits are designed only for feedback stability, and their effects on the performance can be ignored by a proper design, which will be discussed in the next section. In drawing the design guidelines for optimum performance, $Z_{\rm AEF}$ and α are calculated again without the damping circuits for simplification. $Z_{\rm AEF0}$ and α_0, which represent $Z_{\rm AEF}$ and α without the damping circuits, can be expressed as

$$Z_{\rm AEF0} = \frac{Z_{\rm sen} + Z_\pi \left\| \frac{Z_\pi}{\alpha_0} + (R_e + Z_L)\left(Z_\pi \left\| \frac{Z_\pi}{\alpha_0}\right.\right)\left(g_m - \frac{\alpha_0}{Z_\pi}\right)}{1 + \left(Z_\pi \left\| \frac{Z_\pi}{\alpha_0}\right.\right)\left(g_m - \frac{\alpha_0}{Z_\pi}\right)}$$
$$\approx \frac{Z_{\rm sen}}{Z_\pi g_m}\alpha_0 + \frac{1}{g_m} + R_e + \frac{2}{sC_L} + 2R_L \tag{21}$$

where

$$\alpha_0 = \frac{I_x}{I_b} = \frac{Z_{\rm inj} Z_\pi g_m - Z_{\rm sen}}{Z_{\rm sen} + Z_{\rm bias} + Z_{\rm inj}}. \tag{22}$$

$Z_{\rm AEF0}$ can be further simplified at low-frequency and high-frequency ranges.

At the low frequency $Z_{\rm sen} + Z_{\rm inj} > Z_{\rm bias}$, $Z_{\rm AEF0}$ can be simplified as

$$Z_{\rm AEF0,low} \approx Z_{\rm sen} \| Z_{\rm inj} = \frac{1}{s\left(C_{\rm sen} + C_{\rm inj}\right)}. \tag{23}$$

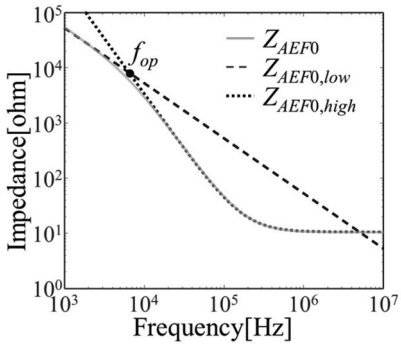

Fig. 7. Impedance of the AEF without the damping circuits $Z_{\rm AEF0}$ (solid lines), the impedance is approximated to $Z_{\rm AEF0,low}$ (dashed lines) and $Z_{\rm AEF0,high}$ (dotted lines) at the low and high frequency ranges, respectively.

Oppositely, at the high frequency $Z_{\rm sen} + Z_{\rm inj} < Z_{\rm bias}$, $Z_{\rm AEF0}$ can also be simplified as

$$Z_{\rm AEF0,high} \approx \frac{Z_{\rm sen} Z_{\rm inj}}{Z_{\rm bias}} + \frac{1}{g_m} + R_e + \frac{2}{sC_L} + 2R_L. \tag{24}$$

$Z_{\rm AEF0,low}$ and $Z_{\rm AEF0,high}$ are overlapped with $Z_{\rm AEF0}$ at the relatively lower and higher frequency ranges, respectively, as shown in Fig. 7.

The boundary frequency between the two ranges $f_{\rm op}$ can be found from $Z_{\rm sen} + Z_{\rm inj} = Z_{\rm bias}$, which is calculated as

$$f_{\rm op} = \frac{C_{\rm sen} + C_{\rm inj}}{2\pi C_{\rm sen} C_{\rm inj} R_{\rm bias}}. \tag{25}$$

Although higher Y-capacitance results in a higher reduction of CM-CEs, the high capacitance also causes a larger leakage current to the earth ground, which is strictly limited by safety regulations. When applying the AEF, however, the Y-capacitance is effectively enlarged in the CE frequency range, but the safety regulation on the leakage current is still satisfied by maintaining the low capacitance at a lower frequency range. In the EMI filter employing the AEF, the Y-capacitance at the low frequency is determined by the sum of $C_{\rm inp}$ and the capacitance produced by (23). Accordingly, the design target of the AEF reduces the values of $Z_{\rm AEF0,high}$ and $f_{\rm op}$ as much as possible while maintaining the sum of $C_{\rm inp}$, $C_{\rm sen}$, and $C_{\rm inj}$ to be under the maximum allowable Y-capacitance $C_{Y,\max}$.

Therefore, the optimized solution for $C_{\rm sen}$ and $C_{\rm inj}$ is given as

$$\left(C_{\rm sen} = C_{\rm inj}\right) \leq 0.5\left(C_{Y,\max} - C_{\rm inp}\right). \tag{26}$$

On the other hand, as aforementioned, the ac utility voltage and DM noises from the EUT can be coupled to the dc supply of the AEF through the two $C_{\rm inj}$ capacitors. When the decoupling capacitor $C_{\rm dc}$ is employed, the coupling transfer function from the power lines to the AEF supply at low frequencies is approximately given as $C_{\rm inj} / \left(C_{\rm inj} + 2C_{\rm dc}\right)$. Since the noise coupling due to the ac utility voltage is usually predominant, a guideline for the value of $C_{\rm dc}$ can be constructed as

$$\frac{C_{\rm inj}}{C_{\rm inj} + 2C_{\rm dc}} V_{\rm ac} < 0.01 V_{\rm dc} \tag{27}$$

where $V_{\rm ac}$ and $V_{\rm dc}$ are the amplitudes of the ac utility voltage and the dc level of the AEF supply, respectively. Equation (27) represents that the coupled noise voltage due to of the ac utility voltage should be less than 1% of $V_{\rm dc}$ to avoid the malfunction of the AEF or control board. The noise-tolerant level can be adjusted as required.

B. BJT Selection and Push–Pull Amplifier Design

The BJTs in the push–pull amplifier should have an operational bandwidth higher than the CEs frequency. Also, the maximum output current of a BJT should be sufficiently larger than the CM noise current I_n for compensation. The small signal current gain of the BJT g_m also contributes to the expression of $Z_{\rm AEF,high}$, as shown in (24); however, the term for $1/g_m$ may be negligible compared to the other terms in a proper design. Therefore, the necessary conditions for BJT specification can be simply summarized as

$$f_T \gg f_H \tag{28}$$

$$I_{c,\max} \gg I_n. \tag{29}$$

f_T and f_H represent the unity current gain bandwidth of a BJT and the high-frequency boundary of the CEs, respectively. $I_{c,\max}$ indicates the maximum limit of the BJT collector current. It is shown in (24) that R_e increases $Z_{\rm AEF0,high}$ and thus degrades AEF performance, but it is necessary to stabilize the BJT bias. The thermal runaway of a BJT also can be prevented by R_e. The typical value of R_e is chosen as 1–4 Ω.

When the maximum noise voltage is applied to the input of the push–pull amplifier, the collector–emitter voltage $V_{\rm ce}$ may approach the saturation region voltage $V_{\rm ce(sat)}$, and the voltage at the BJT emitter becomes $\pm\,(V_{\rm dc}/2 - V_{\rm ce(sat)})$. The maximum output current of the push–pull amplifier $I_{o,\max}$ is then generated as $|V_{\rm dc}/2 - V_{\rm ce(sat)}|/(R_e + 2R_L)$. For proper operation, $I_{o,\max}$ should be adjusted to a setting lower than $I_{c,\max}$ by using R_L. From the relation of $(V_{\rm dc}/2 - V_{\rm ce(sat)})/(R_e + 2R_L) \le I_{c,\max}$, the design guideline of R_L can be extracted as

$$R_L \ge \frac{1}{2I_{c,\max}}\left(\frac{V_{\rm dc}}{2} - V_{\rm ce,sat}\right) - \frac{R_e}{2}. \tag{30}$$

As shown in (24), the magnitude of $Z_{\rm AEF0,high}$ is directly influenced by R_L. Therefore, R_L should be designed as small as possible while satisfying (30). Also, expression (30) indicates that a higher $I_{c,\max}$ of the BJT allows a smaller R_L value, which can improve the AEF performance. Accordingly, the current capacity of BJTs and the value of R_L should be considered simultaneously in the selection of BJTs and R_L.

Next, the bias components of BJTs $R_{\rm bias}$ and R_p are designed. The value of $R_{\rm bias}$ is determined first using (25) with the target $f_{\rm op}$ as

$$R_{\rm bias} = \frac{C_{\rm sen} + C_{\rm inj}}{2\pi C_{\rm sen} C_{\rm inj} f_{\rm op}}. \tag{31}$$

The value of R_p can then be obtained by the dc bias analysis of BJTs. Since the push–pull amplifier is designed as a class AB amplifier, the bias point of each BJT is located slightly above the cutoff. By carrying out KVL from the base to the emitter for a half-portion of the push–pull amplifier, the equation can be derived as

$$\frac{\frac{R_p}{2}}{R_{\rm bias} + \frac{R_p}{2}}\frac{V_{\rm dc}}{2} = I_B\left(R_{\rm bias}\left\|\frac{R_p}{2}\right.\right) + V_{\rm BE} + (I_C + I_B)\,R_e \tag{32}$$

where

$$V_{\rm BE} = V_T\,\ln\frac{I_c}{I_s}. \tag{33}$$

I_C, I_B, and $V_{\rm BE}$ represent the dc collector current, the base current, and the base–emitter voltage, respectively. The value of I_c is selected first to achieve a slight forward bias for each BJT based on the *I–V* curve of the BJTs. The value of R_p can then be extracted by solving (32).

The output of the push–pull amplifier may have a different dc level from the earth ground, and C_L is inserted at the amplifier output as a dc block. Since $Z_{\rm AEF0,high}$ is directly affected by C_L, as shown in (24), the impedance from C_L should be also negligible. If $2/(sC_L) \le Z_{\rm sen}Z_{\rm inj}/Z_{\rm bias}$ is in the target frequency range, (24) can guarantee that the effects of C_L on the AEF performance are negligible. Thus, a convenient quantitative boundary for C_L can be decided as

$$C_L \gg 4\pi f_L C_{\rm sen} C_{\rm inj} R_{\rm bias} \tag{34}$$

where f_L represents the low-frequency boundary of the CEs.

IV. Design Guidelines of the Proposed AEF for Stability and Immunity

The stability and immunity of the proposed AEF should be guaranteed to apply to a real product. As aforementioned, the damping circuits are essential for feedback stability. The damping circuits are already included in expressions (1)–(17). In this section, the design guidelines of the damping circuits are developed step-by-step by investigating their effects on the total loop gain and the AEF impedance $A\beta_t$ and $Z_{\rm AEF}$. Also, the transient immunity standards require that any product should continue to operate correctly after a transient immunity test, such as the lightning surge test. Since the surge test is applied to ac power lines, the components in the AEF can be directly affected by the high voltage transient through the sensing and injection parts. The protection circuits are designed herein to prevent damage from lightning surges.

A. Damping Circuit Design for System Stability

The design of the damping circuits is the most challenging part of the AEF design. As mentioned in Section II-C, system instability of the EMI filter employing the AEF may occur due to the parallel resonance among $Z_{\rm AEF}$, $Z_{\rm inp}$, and $Z_{\rm cm2}$, since the phase of the loop gain, $A\beta_t$ in (16), greatly changes at the resonance frequency $f_{{\rm res},p}$. That is, for the system to be stable, the $A\beta_t$ phase should remain below 180° even at $f_{{\rm res},p}$, as the magnitude of $A\beta_t$ is larger than 0 dB, as shown in Fig. 5(b).

Herein, damping circuits are employed to resolve the feedback stability issue. The proper damping circuits should make the EMI filter stable while maintaining the NA performance.

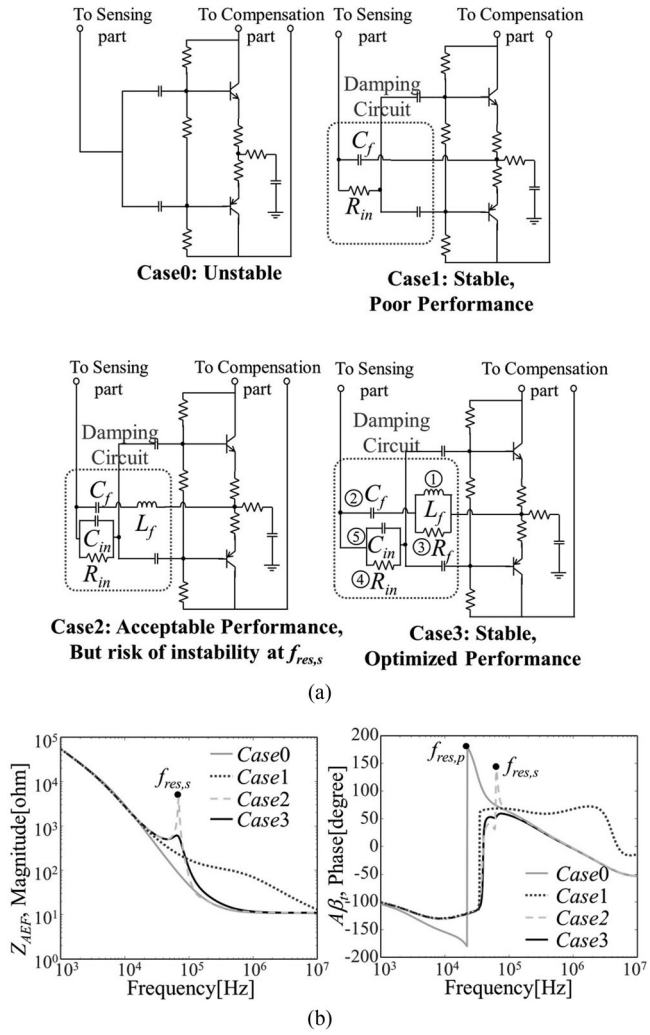

Fig. 8. Investigation of four different configurations of the damping circuits. (a) Circuit schematics (only the AEF parts are drawn for simplicity) and (b) the impedance of the AEF part and the total loop gain $Z_{\rm AEF}$ and $A\beta_t$.

To investigate the role and necessity of each damping circuit element step-by-step, four different cases are tested, as shown in Fig. 8, where only the AEF parts are drawn for simplicity. Note that all other components in the EMI filter remain exactly the same.

Each case in Fig. 8(a) has different configurations of the damping circuits. Starting from the case without any damping circuits, case 0, the stability or performance problems of the AEF are resolved by adding required circuit components. Initially, the EMI filter of case 0 is most likely unstable. Thus, the damping circuits made of C_f and $R_{\rm in}$ are added in case 1, and the filter becomes stable; however, its NA performance is significantly degraded. To recover the NA performance of the filter, L_f and $C_{\rm in}$ are inserted at each damping branch, as shown in case 2. In case 2, however, a risk of instability arises due to the series resonance between L_f and C_f at the resonance frequency $f_{{\rm res},s}$. Therefore, R_f is also added to suppress the Q-factor of the series resonance in case 3. Finally, both stability and performance of the AEF are optimized in case 3.

The stability and performance of the AEF can be accurately identified by observing the AEF impedance and loop gain $Z_{\rm AEF}$ and $A\beta_t$. Those parameters for each case are calculated using (16) and (17) and are plotted in Fig. 8(b). The effects of each damping circuit part, which are explained above, can be clearly observed.

To extract quantitative design guides of the damping circuits, rigorous mathematical analysis is performed. The expressions of $A\beta_t$ and $Z_{\rm AEF}$ in (16) and (17) can be approximated to simpler forms. In the low-frequency range up to $f_{{\rm res},p}$, $A\beta_t$ in (16) can be expressed as

$$A\beta_t \approx Z_\pi \left\| \frac{Z_\pi}{\alpha}\, g_m + \left(1+\frac{Z_{\rm in}}{Z_f}\right)\left(\frac{Z_{\rm sen}}{Z_{\rm cm2}+Z_{\rm LISN}}\right). \quad (35)$$

Also, in the frequency range from f_L to f_H for the CEs, $Z_{\rm AEF}$ in (17) can be approximated as

$$Z_{\rm AEF} \approx \frac{Z_{\rm sen}+Z_f \,\|Z_{{\rm BJT},A}}{1+\left(\frac{Z_f}{Z_f+Z_{{\rm BJT},A}}\right)\left(Z_\pi \,\|\frac{Z_\pi}{\alpha}\right)\left(g_m-\frac{\alpha}{Z_\pi}\right)} + \frac{2}{sC_L}\,\|2R_L \quad (36)$$

where

$$Z_{{\rm BJT},A} = Z_{\rm in} + Z_\pi \left\| \frac{Z_\pi}{\alpha}\,(1+R_e g_m)\right. . \quad (37)$$

$Z_{{\rm BJT},A}$ indicates the approximated expression for $Z_{\rm BJT}$ of (13) in the CEs frequency range.

The damping circuit components are included in $Z_{\rm in}$ and Z_f. When the damping circuits are not applied, as in case 0, the second term of (35) becomes simply $Z_{\rm sen}/(Z_{\rm cm2}+Z_{\rm LISN})$. The phase of $A\beta_t$ in case 0 is close to 180°, as shown in Fig. 8(b), since $A\beta_t$ of case 0 includes a second-order system response due to $Z_{\rm sen}/(Z_{\rm cm2}+Z_{\rm LISN})$. Accordingly, an AEF without any damping circuits would be basically unstable.

Proper damping circuits should make the second term in the loop gain expression (35) be the first-order system to avoid the phase of 180° at the $f_{{\rm res},p}$ frequency. By placing C_f and $R_{\rm in}$ as shown in case 1 of Fig. 8(a), $Z_f = 1/(sC_f)$ and $Z_{\rm in} = R_{\rm in}$. If $R_{\rm in}/(1/(2\pi f_{{\rm res},p}C_f)) > 1$, then the second term of (35) behaves as the first-order system by cancelling the effect of $Z_{\rm sen}$ using Z_f. Therefore, in case 1, the phase of the loop gain $A\beta_t$ does not reach 180° and the EMI filter with AEF can stay stable. As a result, the relationship between C_f and $R_{\rm in}$ can be extracted from the condition for stability $R_{\rm in}/(1/(2\pi f_{{\rm res},p}C_f)) > 1$ at $f_{{\rm res},p}$ as

$$R_{\rm in} \geq \frac{1}{2\pi f_{{\rm res},p}C_f} \quad (38)$$

where

$$f_{{\rm res},p} \approx \frac{1}{2\pi\sqrt[3]{C_{\rm sen}C_{\rm inj}R_{\rm bias}\,(L_{\rm cm2}+M_{\rm cm2})}}. \quad (39)$$

Another design rule of C_f will be presented later using case 2 of Fig. 8(a), since the design rule of C_f is associated with other parameters in the damping circuits.

The effects of the damping circuits in case 1 on $Z_{\rm AEF}$ should also be investigated. $Z_{{\rm BJT},A}$ of (37) is increased by $R_{\rm in}$

compared to that without damping circuits. Then, the denominator of the first term in (36) approaches "1" because Z_f is much smaller than $Z_{\mathrm{BJT},A}$ in the CEs frequency range. Accordingly, Z_{AEF} in case 1 maintains a high impedance close to $(Z_{\mathrm{sen}} + Z_f + (2/(sC_L))||2R_L)$ in the target frequency range. In other words, the effective capacitance of Z_{AEF} is not increased when the damping circuits C_f and R_{in} are employed, as shown in Fig. 8(b).

To resolve the NA performance degradation due to the damping circuits, Z_f should remain greater than $Z_{\mathrm{BJT},A}$. Also, Z_{in} should be smaller than the other term in $Z_{\mathrm{BJT},A}$ of (37) to suppress the effect of R_{in} on Z_{AEF}. For these reasons, L_f is added in series at the impedance Z_f, and C_{in} is added in parallel at Z_{in}, as shown in case 2 of Fig. 8(a). By adjusting the values of L_f and C_{in}, the increased effective capacitance of Z_{AEF} can be achieved in the frequency range of the CEs, as shown in case 2 of Fig. 8(b).

Quantitatively, the impedance of L_f should be larger than Z_π to achieve the condition of $(Z_f > Z_{\mathrm{BJT},A})$, since L_f and Z_π have dominant impedances in Z_f and $Z_{\mathrm{BJT},A}$, respectively. The design rule for L_f can be found at the low-frequency limit for the CEs f_L as

$$L_f > \frac{1}{4\pi f_L}\left(r_\pi \left\| \frac{1}{2\pi f_L C_\pi}\right.\right). \tag{40}$$

Similarly, the impedance of C_{in} should be smaller than Z_π at the frequency f_L, as $1/(2\pi f_L C_{\mathrm{in}}) < r_\pi||(1/(2\pi f_L C_\pi))$.

For the stability to still be retained, the effects of L_f and C_{in} at the frequency $f_{\mathrm{res},p}$ should be negligible. That is, the impedance of C_f at $f_{\mathrm{res},p}$ should be sufficiently larger than that of L_f. For convenience sake, a design guide can be drawn from $1/(2\pi f_{\mathrm{res},p} C_f) \geq 5\,(2\pi f_{\mathrm{res},p} L_f)$ as

$$C_f \leq \frac{1}{20\pi^2 f_{\mathrm{res},p}^2 L_f}. \tag{41}$$

Also, the impedance of C_{in} should be sufficiently larger than R_{in}, as $1/(2\pi f_{\mathrm{res},p} C_{\mathrm{in}}) \geq 5R_{\mathrm{in}}$. Considering both conditions for C_{in} regarding the performance $(1/(2\pi f_L C_{\mathrm{in}}) \leq r_\pi||(1/(2\pi f_L C_\pi)))$ and the stability $(1/(2_\pi f_{\mathrm{res},p} C_{\mathrm{in}}) \geq 5R_{\mathrm{in}})$, the design guideline of C_{in} can be summarized as

$$\frac{1}{2\pi f_L\,(r_\pi \,\|1/\,(2\pi C_\pi f_L))} \leq C_{\mathrm{in}} \leq \frac{1}{10\pi f_{\mathrm{res},p} R_{\mathrm{in}}}. \tag{42}$$

When the damping circuit components are designed based on (38) and (40)–(42), a stable AEF system with acceptable performance can be achieved in the CEs frequency range, as shown in case 2 of Fig. 8(b).

A final trim is still needed in the damping circuit design, however. A series resonance occurs between L_f and C_f. At the resonance frequency $f_{\mathrm{res},s}$, the magnitude of Z_f is minimized and the phase abruptly changes. If the minimum Z_f at $f_{\mathrm{res},s}$ is much smaller than $Z_{\mathrm{BJT},A}$, a peak of Z_{AEF} occurs, as shown in Fig. 8(b), since the denominator of the first term in (37) is close to "1." Also, the phase of the loop gain $A\beta_t$ abruptly increases at $f_{\mathrm{res},s}$ through a rapid phase variation of Z_f. Accordingly, the variation of Z_f at the $f_{\mathrm{res},s}$ frequency should be mitigated by adjusting the quality factor of the series resonance. Hence, R_f is added in parallel with L_f to adjust the quality (Q) factor, as shown in case 3 of Fig. 8. Both the performance degradation and the instability risk at $f_{\mathrm{res},s}$ can be mitigated by designing the Q factor, which is expressed as $R_f/(2\pi f_{\mathrm{res},s} L_f)$, to be smaller than 10. The purpose of R_f is only to reduce the Q-factor without affecting the roles of other damping circuit components. Thus, R_f should be sufficiently larger than the impedance of L_f at $f_{\mathrm{res},p}$, such that $R_f \geq 5 \cdot (2\pi f_{\mathrm{res},p} L_f)$. In summary, the design guides for R_f can be extracted as

$$10\pi f_{\mathrm{res},p} L_f \leq R_f \leq 20\pi f_{\mathrm{res},s} L_f \tag{43}$$

where

$$f_{\mathrm{res},s} = \frac{1}{2\pi\sqrt{L_f C_f}}. \tag{44}$$

Finally, after R_f is designed based on (43) and applied in the damping circuits, both stability and performance are optimized, as shown in case 3 of Fig. 8(b).

Physically, the role of each damping circuit component so far can be summarized as follows. The amplifier input voltage is attenuated by R_{in} at the $f_{\mathrm{res},p}$ frequency for stability. The noise voltages in the CEs frequency range can be still applied well to the amplifier input through C_{in} for performance. C_f is the phase compensation capacitor for stability. The large impedance of R_f and L_f make the phase compensation path invisible in the CEs frequency range for performance.

In practical designs, all the values of the damping circuit components can be easily designed by selecting the L_f value first, since L_f in (40) is only a function of the BJT parameters. The most convenient order for selecting component values is denoted by the numbers in circles in the figure for case 3 in Fig. 8(a).

The maximum phase of the loop gain over the whole frequency range is calculated using (16) and is plotted by sweeping the value of each damping circuit component, as shown in Fig. 9. The values of all other components except for the swept value are fixed to the designed values. In Fig. 9(a), a C_f value smaller than 27 nF or larger than 38 nF can cause system instability by violating design rule (38) or (41). The unstable ranges due to the value of R_f in Fig. 9(b) are attributed to (43). Although there are both low and high limits in choosing the value of C_{in}, as (42), system instability occurs only at a large C_{in} exceeding the high boundary, as shown in Fig. 9(c), since the low boundary is due to NA performance. In the case of R_{in}, system instability is caused by violating design rules (38) and (42), as shown in Fig. 9(d). The increase of C_f and R_{in} allows the AEF to be more stable by decreasing the maximum phase in the whole frequency range, as shown in Fig. 9(a) and (d). When R_{in} and C_f are adjusted for system stability, all other components in the damping circuits also should be redesigned according to the design guides, since all the damping circuit components are related to each other.

The effects of the damping circuits on the stability can be demonstrated by measuring the CM noise at the LISN side after removing the damping circuits in the AEF. Fig. 10(a) and (b) shows the results measured in both time and frequency domains using an oscilloscope and a spectrum analyzer, respectively. In the measurements, the EUT was turned OFF while only the AEF

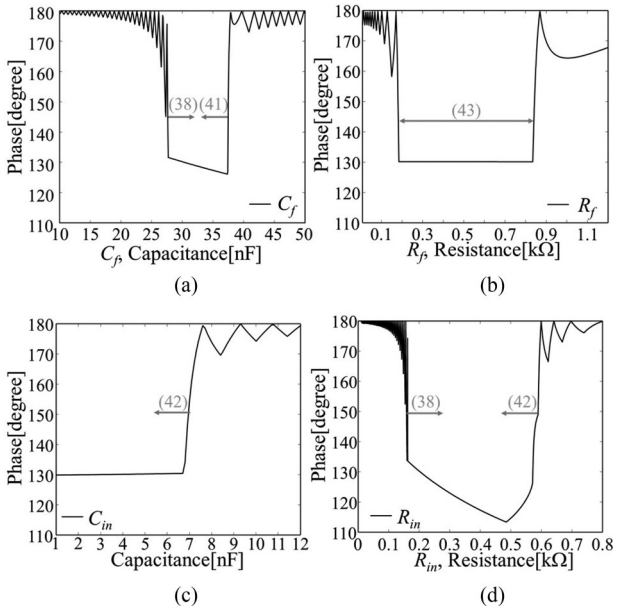

Fig. 9. Maximum phase of the loop gain $A\beta_t$ while sweeping the value of (a) C_f, (b) R_f, (c) $C_{\rm in}$, and (d) $R_{\rm in}$.

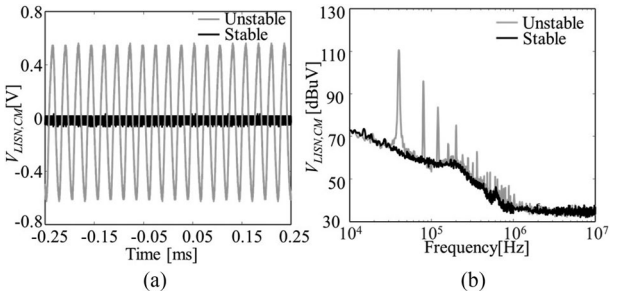

Fig. 10. CM noise with and without the damping circuits (a) in the time-domain measurements and (b) in the frequency-domain measurements.

turned on. Without the damping circuits, the oscillation due to the instability occurs, creating the peaks at its harmonics in the frequency spectrum. After applying the damping circuits, all the oscillations and harmonic peaks disappear, as shown in Fig. 10. The damping circuits are an essential part in the proposed AEF.

B. Surge Protection Circuit Design

The high voltage transient caused by a lightning surge can physically damage the components of power converters inside appliances. Generally, protectors such as metal oxide varistor and gas discharge tubes are additionally installed prior to the EMI filter for overvoltage clamping, denoted as M_1, M_2, and GDT in Fig. 11. However, the clamping voltage of the varistor and GDT in front of the EMI filter are usually very high—as much as several kV—to avoid interrupting the normal operation of the power system. Hence, despite the presence of those protectors, an overvoltage of several kV can be still generated and applied to the AEF.

When the lightning surge occurs, the overvoltage between collector and emitter nodes can damage the BJTs. Furthermore,

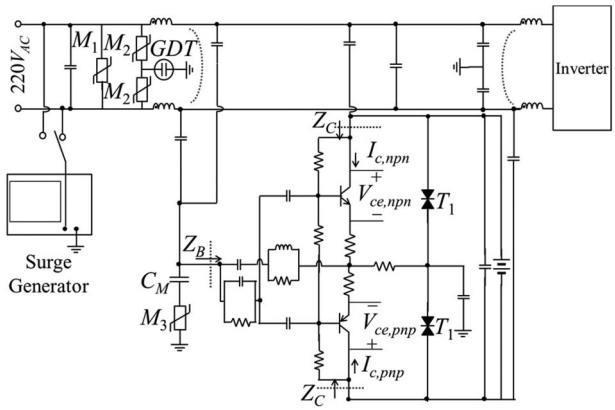

Fig. 11. Proposed surge protection circuits for the AEF.

an overcurrent can flow between the power lines and earth ground through R_e, R_L, $R_{\rm in}$, R_f, and BJTs. The passive components in the AEF should also be protected from the high-power transient, requiring additional protection circuits in the AEF side. The protection circuits are implemented using the varistor at the input side of the AEF M_3 and the transient voltage suppression (TVS) diodes T_1 and T_2, along both NPN and PNP BJTs, respectively, as shown in Fig. 11. The TVS diodes for protecting the BJTs are chosen to have a lower clamping voltage and a faster response compared to the varistor, whereas the varistor M_3 at the amplifier input is chosen to dissipate a high current and high energy. The varistor at the amplifier input can be also replaced by a TVS diode if a fast response is required.

The bidirectional TVS diodes T_1 protect the BJTs and passive components from the high voltage transient. Since the voltage across T_1 is limited by the clamping voltage of T_1, V_{T1}, V_{T1} should be lower than the maximum collector–emitter voltage tolerance $V_{\rm CE,max}$, but higher than $V_{\rm dc}$ in order not to interrupt the normal AEF operation. Accordingly, the condition for choosing V_{T1} can be simply written as

$$V_{\rm dc} < V_{T1} < V_{\rm CE,max}. \tag{45}$$

M_3 protects the passive components at the amplifier input side against the high voltage transient. The dc block capacitor C_M is also added between $C_{\rm sen}$ and M_3 to avoid any unwanted operation of M_3 due to a dc voltage difference between the sensing node and the earth ground. If the high voltage transients are generated, M_3 should operate below the rating voltage of the passive components that are placed at the amplifier input. Assuming the lowest rating voltage in the passive components is $V_{\rm passive,rate}$, the condition for the clamping voltage of M_3, V_{M3}, is conveniently given as

$$V_{M3} < V_{\rm passive,rate}. \tag{46}$$

The parasitics in the varistor and TVS diode can degrade the performance of the proposed AEF. The characteristics of the protection devices at the idle state in the CEs frequency range should be dominated by parasitic capacitance. Thus, the parasitic capacitance in the varistor and TVS should be also considered in selecting the protection devices. By naming the parasitic capacitance of M_3 and T_1 as $C_{{\rm para},M3}$ and $C_{{\rm para},T1}$,

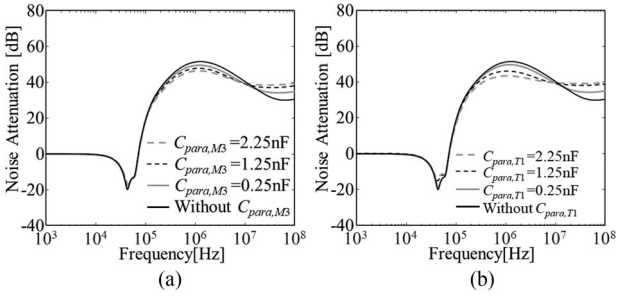

Fig. 12. NA according to the parasitic capacitance in the (a) varistor M_3 and (b) TVS diode T_1.

respectively, the impedance of the protection devices can be written as

$$Z_{\mathrm{para},M3} = \frac{1}{sC_{\mathrm{para},M3}}, Z_{\mathrm{para},T1} = \frac{1}{sC_{\mathrm{para},T1}}.$$

Also, the impedances looking at the input and the collector nodes of the push–pull amplifier with reference to the earth ground are named as Z_B and Z_C, respectively, as shown in Fig. 11. In the CEs frequency range, Z_{in} and C_L are negligible, and Z_B and Z_C can be expressed as

$$\begin{aligned} Z_B &= \frac{V_B}{I_b + I_x + I_f} = Z_{\mathrm{BJT}} \| Z_f + Z_{L,\mathrm{FB}} \\ &\approx \left(1 + \frac{2R_L g_m}{1 + R_e g_m}\right) \left(R_f \left\| \frac{Z_\pi}{1+\alpha}(1 + R_e g_m)\right.\right) \\ Z_C &= \frac{V_C}{I_o - I_x} \approx -\left(Z_{\mathrm{bias}} - \frac{Z_\pi}{\alpha}\right) \frac{I_x}{I_o - I_x} \approx -Z_{\mathrm{inj}} \end{aligned}$$

where α given in (1) also can be approximated to $(Z_{\mathrm{inj}} Z_\pi g_m / Z_{\mathrm{bias}})$.

To avoid the performance degradation of the AEF, the currents flowing through M_3 and T_1 should be smaller than the currents into the base and the collector of the BJTs, respectively, in the CEs frequency range. Accordingly, Z_B and Z_C should be sufficiently smaller than $Z_{\mathrm{para},M3}$ and $Z_{\mathrm{para},T1}$, respectively, until the upper boundary of the CEs frequency range f_H. From these conditions, the boundaries for $C_{\mathrm{para},M3}$ and $C_{\mathrm{para},T1}$ can be extracted as

$$C_{\mathrm{para},M3} < \frac{1}{2\pi f_H \left(1 + \frac{2R_L g_m}{1+R_e g_m}\right) \left(R_f \left\| \frac{Z_\pi}{1+\alpha}(1 + R_e g_m)\right.\right)} \tag{47}$$

$$C_{\mathrm{para},T1} < C_{\mathrm{inj}}. \tag{48}$$

The boundaries of (47) and (48) are calculated as 500 pF and 1.5 nF for the designed AEF circuit, respectively. To validate the effects of $C_{\mathrm{para},M3}$ and $C_{\mathrm{para},T1}$ on the AEF performance, the NA was calculated with varying the value of each parasitic capacitance from 0.25 to 2.25 nF, as shown in Fig. 12. When the values of $C_{\mathrm{para},M3}$ and $C_{\mathrm{para},T1}$ approach the boundaries of (47) and (48), the performance of the proposed AEF is actually degraded. $C_{\mathrm{para},T1}$ has a larger effect on the performance degradation than $C_{\mathrm{para},M3}$, and the protection circuit in the collector side should be more carefully selected.

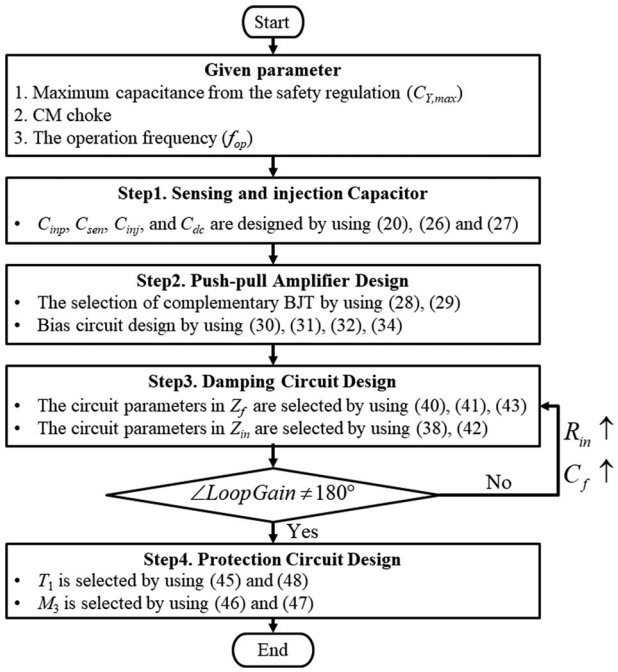

Fig. 13. Design flow of the proposed AEF.

V. Implementation and Measurements of the Proposed AEF

A. Design Flow and Implementation

The design flow for the proposed AEF is summarized in Fig. 13. Assume that maximum allowable Y-capacitance $C_{Y,\max}$ and the CM chokes to be used are given prior to the design of AEF. The f_{op} frequency is just chosen to be sufficiently lower than the low boundary of the CEs frequency range. The equivalent capacitance of the CM noise source C_n can be extracted from the measured CEs of the EUT [32]–[34]. At step 1 of Fig. 13, C_{inp}, C_{sen}, C_{inj}, and C_{dc} are designed from (20), (26), and (27). At step 2, the BJTs are chosen based on (28) and (29), and the bias and output components of the AEF R_{bias} R_p, R_L, and C_L are determined using (30)–(32). The damping circuits are then designed at step 3. The parallel resonance frequency $f_{\mathrm{res},p}$ is calculated first, with the designed values of L_{cm2}, C_{sen}, C_{inj}, and R_{bias} using (39). The damping branch composed of L_f, R_f, and C_f are designed using (40), (41), and (43). Then, the other damping branches for R_{in} and C_{in} are determined using (38) and (42). After the prototype design of the damping circuits, the stability of the overall filter with the proposed AEF should be confirmed by checking the phase of the loop gain. If the proposed AEF is unstable, the damping circuits should be redesigned after increasing R_{in} or C_{in}. At step 4, the surge protection circuits are employed according to the design rules of (45)–(48).

The total EMI filter with the proposed AEF has been designed according to the design flow, and then manufactured in a printed circuit board (PCB) at a size of 53 mm by 53 mm, as shown in Fig. 14. All component values in the proposed AEF are summarized in Table I. In the proposed AEF, the high voltage rating Y-type capacitors were used for the capacitors connected

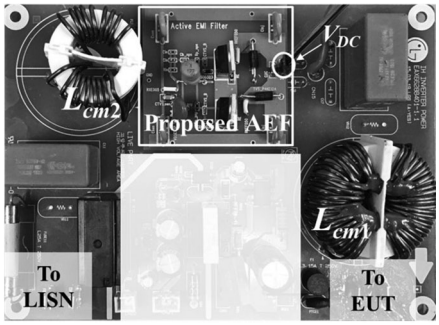

Fig. 14. Photograph of the total EMI filter with the proposed AEF.

TABLE I
COMPONENTS VALUES OF THE PROPOSED ACTIVE EMI FILTER

Components	Values
$C_{\rm sen}$, $C_{\rm inj}$, C_b, $C_{\rm inp}$, $C_{\rm dc}$	1.5 nF, 1.5 nF, 1 μF, 0.47 nF, 2.2 μF
$R_{\rm bias}$, R_p	33 kΩ, 7.7 kΩ
R_e, R_L, C_L	2 Ω, 2.2 Ω, 140 nF
$R_{\rm in}$, $C_{\rm in}$	200 Ω, 5 nF
R_f, C_f, L_f	330 Ω, 30 nF, 200 μH
$L_{\rm cm1}$, $R_{\rm cm1}$, $C_{\rm cm1}$	8 mH, 80 kΩ, 10 pF
$L_{\rm cm2}$, $R_{\rm cm2}$, $C_{\rm cm2}$	1 mH, 4 kΩ, 16 pF

to the power lines $C_{\rm inj}$, $C_{\rm sen}$, and $C_{\rm inp}$, which have a relatively large tolerance. It has been validated by simulations that the performance and stability are rarely affected by the change of Y-capacitor values within 20% tolerance. They are not main contributors to the performance or stability of the AEF. The circuit models of the CM choke are extracted using the VNA measurements. The BJTs, KSA473 and KSC1173, and the surge protection circuits, P6KE22CA and V05E95P, have been used. V_{T1} and V_{M3} of the protection circuits are 22 and 150 V, respectively. C_M is set as 1μF. In the product example, a dc 18 V supply voltage for the proposed AEF was available from the control board of the main power system, which is usually the case in real products. Otherwise, a proper dc power supply should be separately implemented for the AEF. When a dc of 18 V is supplied for the power of the AEF, the average operating current of the proposed AEF is measured as 16 mA. Accordingly, the total power consumption of the operating AEF is about 288 mW in average. The power loss due to all passive resistors in the AEF was also found by measuring the applied voltages at each resistor, which was calculated as 12.4 mW. As a result, the power loss due to the passive resistors is quite small as about 4.3% of the total power consumption of the AEF.

B. VNA Measurements for Performance Validation

The performance of an EMI filter can be estimated from VNA measurements. The EMI filter with the proposed AEF is compared to the filter with passive Y-capacitors. The value of the passive Y-capacitor C_Y is set as the sum of $C_{\rm sen}$, $C_{\rm inj}$, and $C_{\rm inp}$, which are utilized in the filter with the proposed AEF.

In the VNA measurements, the noise source and noise receiver are assigned as port1 and port2, respectively, as shown in Fig. 15(a). The S_{21} parameters representing the propagated signal from port1 to port2 are measured and plotted in Fig. 15(b). S_{21} simulated by SPICE is also plotted, validating the modeling accuracy up to 10 MHz. By employing an AEF in the EMI filter instead of the passive Y-capacitor, S_{21} is reduced by about 10–20 dB in a frequency range from 100 kHz to 6 MHz, as shown in Fig. 15(b).

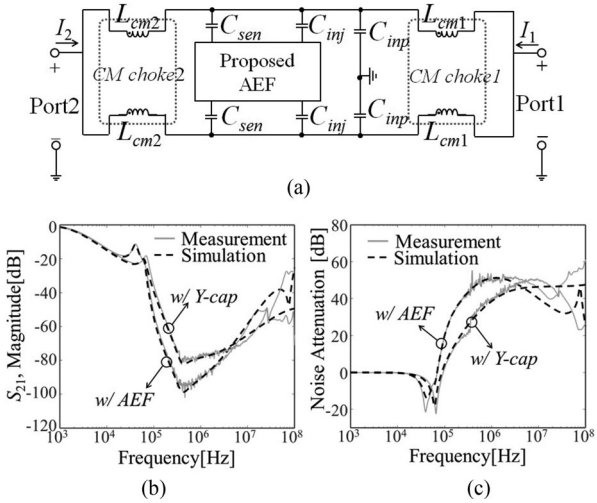

Fig. 15. (a) Schematics of a VNA measurement, (b) S_{21} parameter with the proposed AEF and with the PEF, and (c) measured NA with the proposed AEF and with the PEF.

The NA can also be extracted from the *Z* parameters measured by the VNA as

$$\mathrm{NA} = -\frac{I_1}{I_2} = -\frac{Z_{\rm LISN} + Z_{11}}{Z_{12}} \tag{49}$$

where I_1 and I_2 represent the input currents at port1 and 2, respectively. The NA extracted from the VNA measurement is also compared to that which was simulated by SPICE in Fig. 15(c). The simulated NA is exactly the same as those calculated using (18) and (19). $\mathrm{NA}_{\rm AEF}$ is higher than $\mathrm{NA}_{\rm Y-cap}$ by about 10–20 dB in a frequency range from 100 kHz to 6 MHz, which correlates with the S_{21} comparison.

C. Measurement in a Real Application in a Product

The EMI filter with the proposed AEF was installed in front of the 2.2 kW current resonance inverter in a commercial product. For comparison, the filter with the passive Y-capacitors and the filter without either the AEF or Y-capacitors have also been tested in the same setup. The CM-CEs for all cases are measured by using LISN, CM/DM separator, and spectrum analyzer in the frequency range from 150 kHz to 30 MHz, as shown in Fig. 16(a). After applying the EMI filter with the proposed AEF to the real product, the CEs are attenuated by about 5–25 dB in the frequency range from 150 kHz to 6 MHz, as compared to the case without any filter. The case of the EMI filter with the AEF also shows less CEs than that with the Y-capacitors by about 5–15 dB from 150 kHz to 6 MHz, which is consistent with the results from VNA measurements. The EMI filter with the proposed AEF has effectively reduced the CM-CEs below

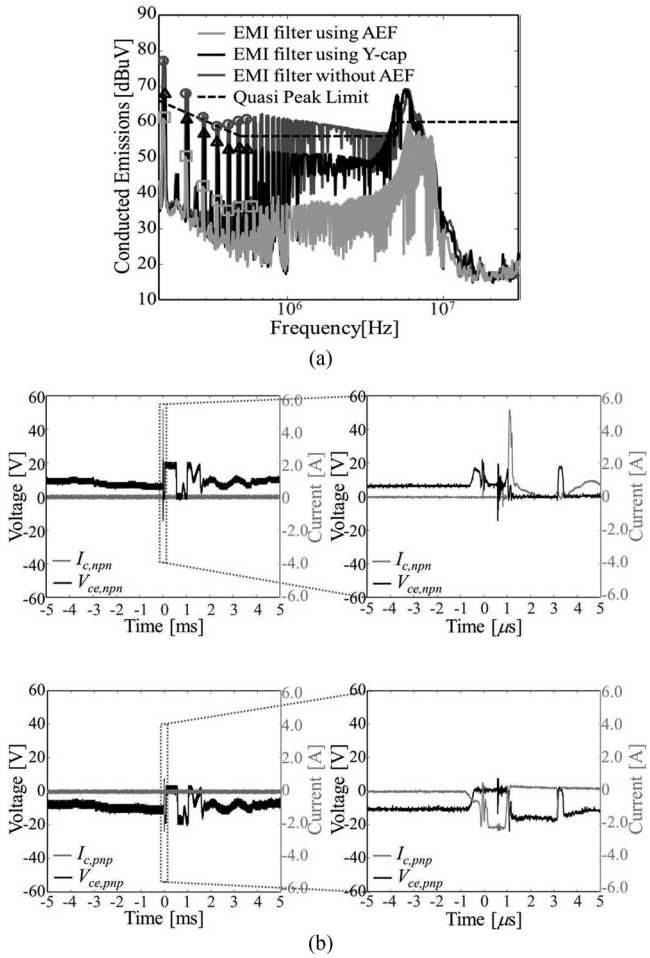

Fig. 16. (a) CM-conducted emissions measurement result and (b) BJT voltages and currents measured during the lightning surge test.

the quasi-peak limit of the CISPR-Class B regulation, as shown in Fig. 16(a). However, the EMI peaks at about 7 MHz are not much decreased by the AEF. The high EMI peaks at a narrow frequency band above several MHz are usually attributed to the resonance between the noise source impedance and a shunt capacitance to the ground. Thus, the EMI filter can rarely suppress the resonance, but is involved in the resonance. Accordingly, an additional method should be necessary to suppress the 7-MHz CEs under the regulations with a sufficient margin.

At the resonance frequency between the noise source impedance and the EMI filter, the CEs are highly related to the quality factor of the resonance path. Therefore, a damping component suppressing the resonance can effectively reduce the EMI peaks. A ferrite bead is commonly utilized as the damping component [2]. An impedance mismatching filter consisting of a CM choke and a resistor has also been introduced in [36]. Furthermore, adding a Y-capacitor at the LISN side is also a possible solution to improve the NA at the high frequencies, which modifies the total EMI filter topology of the *L–C–L* configuration to the double *L–C* filter.

The low-frequency CM-CEs are usually more difficult to reduce when using the passive EMI filters, which require larger and expensive CM chokes. Hence, the proposed AEF has been designed in the purpose to demonstrate the reduction of CEs predominantly in the low-frequency range. As a result, the CEs have been effectively attenuated by the AEF without increasing the leakage current and adding any bulky CM chokes.

To demonstrate the protection circuits, the BJT voltages and currents were measured while the CM surge test was being performed, as shown in Fig. 11. The 2 kV peak, 1.2 μs /50 μs open-circuit voltage and the 8 μs /20 μs short-circuit current are generated by the surge generator (UCS 500N) [35]. After the CM surge voltage is excited, the voltages between the collector and emitter at each BJT $V_{\mathrm{ce,npn}}$ and $V_{\mathrm{ce,pnp}}$ fluctuate but do not exceed V_{T1} due to the behavior of T_1, as shown in Fig. 16(b). The BJT collector currents $I_{c,\mathrm{npn}}$ and $I_{c,\mathrm{pnp}}$ are also induced but do not exceed the rate of the BJTs.

Also, when the BJT collector current flows, $V_{\mathrm{ce,npn}}$ or $V_{\mathrm{ce,pnp}}$ decreases near 0 V due to the voltage drop at R_e, as shown in Fig. 16. Accordingly, the power dissipation at the BJTs is quite low, falling below the safe operating area. Thus, the proposed AEF can withstand the high voltage transient and behave well after the surge tests.

D. Discussion

The performances and characteristics of several previous AEFs are compared with the proposed AEF, as summarized in Table II. The max attenuation of the AEF in the CEs measurement $\mathrm{ATT}_{\max}$ is defined as

$$\mathrm{ATT}_{\max} = \max\left(\frac{CE_{\mathrm{w/oAEF}}(f)}{CE_{\mathrm{w/AEF}}(f)}\right).$$

$\mathrm{CE}_{\mathrm{w/oAEF}}$ and $\mathrm{CE}_{\mathrm{w/AEF}}$ are designated as the CEs without and with the AEF, respectively. $\mathrm{ATT}_{\max}$ of each AEF is presented in Table II, based on the presented value in each reference. The inductive coupling and capacitive coupling are performed by using a transformer and capacitor, respectively. Although the low-frequency boundary of the attenuation in the proposed AEF is quite higher than those of the AEFs in [13] and [17], the proposed AEF provides a higher attenuation in the frequency range from 150 kHz to 7 MHz in the CEs regulation range. Regarding the size, weight, and cost, the proposed AEF should be the smallest, lightest, and cheapest, since the low-cost BJTs with a low voltage rating are utilized without any transformers, which is usually the most expensive component. For example, the AEF in [17] includes a small core with the diameter of 10 mm and the weight of 179 g, which is already much heavier than the total weight of the proposed AEF, 19 g. The proposed AEF can be very easily embedded inside a real product without increasing the size and cost.

As mentioned in Section II-C, however, the leakage current should be considered in the design of the proposed AEF. Also, as another drawback as compared to the AEF in [17], the proposed AEF requires a separate dc supply, although a proper dc voltage is usually available from a control board in real application products.

TABLE II
COMPARISON OF PERFORMANCES AND CHARACTERISTICS BETWEEN AEFS

	Sensing-injection type	Type of Amp.	Bandwidth [MHz]	ATT_{max} [dB]	Target EUT [kW]	Size and weight	Benefits	Drawbacks
[13]	Inductive–Capacitive	Op Amp	0.010–6	30	1	Transformer, Active components dependent	*ATT.* in a low-frequency range Higher DOF in amp design	Bulky and expensive transformer Additional dc supply
[14]	Capacitive–Inductive	Op Amp	0.150–10	12	0.2	Transformer, Active components dependent	Low leakage current Higher DOF in amp design	Bulky and expensive transformer Additional dc supply
[17]	Capacitive–Inductive	Push–pull Amp	0.010–3	20	3.7	Transformer, Active components dependent	*ATT.* in a low-frequency range Standalone	Bulky and expensive transformer High-voltage BJT
[21]	Inductive–Capacitive	Push–pull Amp.	0.150–10	20	3.7	Transformer, Active components dependent	Low-voltage BJT	Bulky and expensive transformer Additional dc supply
This work	Capacitive–Capacitive	Push–pull Amp.	0.150–6	25	2.2	Active components dependent	Low-voltage BJT Compact and light	Leakage current Additional dc supply

VI. CONCLUSION

The novel features of the proposed AEF can be characterized as 1) the push–pull amplifier with the low voltage rating BJTs, 2) transformerless, and 3) direct analog noise sensing. The AEF was completely analyzed and expressed by the block diagram based on a circuit analysis. The loop gain has been effectively extracted from the block diagram to determine the system stability.

Quantified practical design guidelines were rigorously derived from the analysis with considerations for both performance and stability. For practical applications in commercial products, immunity to high voltage transient also was taken into account, and the design rules of the protection circuits were presented. The design flow of the AEF was built based on the extracted design rules. The total EMI filter with the proposed AEF was designed according to the design flow and implemented in a compact size PCB. The performance of the filter with AEF was verified with VNA measurements. The AEF was applied to a commercial product with the 2.2 kW current resonance inverter, and the CM-CEs were effectively attenuated by about 5–25 dB from 150 kHz to 6 MHz without increasing the leakage current or adding any bulky CM chokes. The immunity of the proposed AEF was also demonstrated with the 2 kV CM surge tests.

Structurally, the transformerless AEF is free from the magnetic saturation caused by a high current and can be easily built in a compact size. The proposed AEF shows promise in resolving the size and cost problems of the EMI filter due to CM chokes, especially in high power applications. Since immunity against high voltage transients was also verified, the proposed AEF is ready to be applied in real-world fields.

REFERENCES

[1] K. Mainali and R. Oruganti, "Conducted EMI mitigation techniques for switch-mode power converters: A survey," *IEEE Trans. Power Electron.*, vol. 25, no. 9, pp. 2344–2356, Sep. 2010.

[2] C. Paul, *Introduction to Electromagnetic Compatibility*, 2nd ed., Hoboken, NJ, USA: Wiley, 2006.

[3] L. Tihanyi, *Electromagnetic Compatibility in Power Electronics*. New York, NY, USA: IEEE Press, 1995.

[4] O. M. Timothy and P. L. Richard, *EMI Filter Design*, 3rd ed. Boca Raton, FL, USA: CRC Press, 2011.

[5] H. Chen, Z. Qian, S. Yang, and C. Wolf, "Finite-element modeling of saturation effect excited by differential-mode current in a common-mode choke," *IEEE Trans. Power Electron.*, vol. 24, no. 3, pp. 873–877, Mar. 2009.

[6] M. J. Nave, "On modeling the common mode inductor," in *Proc. IEEE Int. Symp. Electromagn. Compat.*, Aug. 1991, pp. 452–457.

[7] L. LaWhite and M. F. Schlecht, "Active filters for 1-MHz power circuits with strict input/output ripple requirements," *IEEE Trans. Power Electron.*, vol. PE-2, no. 4, pp. 282–290, Oct. 1987.

[8] L. LaWhite and M. F. Schlecht, "Design of active ripple filters for power circuits operating in the 1–10 MHz range," *IEEE Trans. Power Electron.*, vol. 3, no. 3, pp. 310–317, Jul. 1988.

[9] N. K. Poon, J. C. P. Liu, C. K. Tse, and M. H. Pong, "Techniques for input ripple current cancellation: Classification and implementation," *IEEE Trans. Power Electron.*, vol. 15, no. 6, pp. 1144–1152, Nov. 2000.

[10] Y. Son and S. Sul, "Generalization of active filters for EMI reduction and harmonics compensation," *IEEE Trans. Ind. Appl.*, vol. 42, no. 2, pp. 545–551, Mar./Apr. 2006.

[11] K. Mainali and R. Oruganti, "Design of a current-sense voltage-feedback common mode EMI filter for an off-line power converter," in *Proc. IEEE Power Electron. Spec. Conf.*, 2008, pp. 1632–1638.

[12] W. Chen, W. Zhang, X. Yang, Z. Sheng, and Z. Wang, "An experimental study of common- and differential-mode active EMI filter compensation characteristics," *IEEE Trans. Electromagn. Compat.*, vol. 51, no. 3, pp. 683–691, Aug. 2009.

[13] W. J. Chen, X. Yang, and Z. Wang, "A novel hybrid common-mode EMI filter with active impedance multiplication," *IEEE Trans. Ind. Electron.*, vol. 58, no. 5, pp. 1826–1834, May 2011.

[14] D. Shin *et al.*, "Analysis and design guide of active EMI filter in a compact package for reduction of common-mode conducted emissions," *IEEE Trans. Electromagn. Compat.*, vol. 57, no. 4, pp. 660–671, Aug. 2015.

[15] M. L. Heldwein, H. Ertl, J. Biela, and J. W. Kolar, "Implementation of a transformerless common-mode active filter for offline converter systems," *IEEE Trans. Ind. Electron.*, vol. 57, no. 5, pp. 1772–1786, May 2010.

[16] Y. Chu, S. Wang, and Q. Wang, "Modeling and stability analysis of active/hybrid common-mode EMI filters for dc/dc power converters," *IEEE Trans. Power Electron.*, vol. 31, no. 9, pp. 6254–6263, Sep. 2016.

[17] S. Ogasawara, H. Ayano, and H. Akagi, "An active circuit for cancellation of common-mode voltage generated by a PWM inverter," *IEEE Trans. Power Electron.*, vol. 13, no. 5, pp. 835–841, Sep. 1998.

[18] M. C. Di Piazza, G. Tinè, and G. Vitale, "An improved active common-mode voltage compensation device for induction motor drives," *IEEE Trans. Ind. Electron.*, vol. 55, no. 4, pp. 1823–1834, Apr. 2008.

[19] M. C. Di Piazza, A. Ragusa, and G. Vitale, "Design of grid-side electromagnetic interference filters in ac motor drives with motor-side common mode active compensation," *IEEE Trans. Electromagn. Compat.*, vol. 51, no. 3, pp. 673–682, Aug. 2009.
[20] M. C. Di Piazza, A. Ragusa, and G. Vitale, "Effects of common mode active filtering in induction motor drives for electric vehicles," *IEEE Trans. Veh. Technol.*, vol. 59, no. 6, pp. 2664–2673, Sep. 2010.
[21] Y. Son and S. Sul, "A new active common-mode EMI filter for PWM inverter," *IEEE Trans. Power Electron.*, vol. 18, no. 6, pp. 1309–1314, Nov. 2003.
[22] K. Euerle, K. Iyer, E. Severson, R. Baranwal, S. Tewari, and N. Mohan, "A compact active filter to eliminate common-mode voltage in a SiC-based motor drive," in *Proc. 2016 IEEE Energy Convers. Congr. Expo.*, 2016, pp. 1–8.
[23] A. Esmaeli, Y. Sun, and L. Sun, "Mitigation of the adverse effects of PWM inverter through active filter technique," in *Proc. 1st Int. Symp. Syst. Control Aerosp. Astronaut.*, Jan. 2006, p. 774.
[24] P. Pairodamonchai, S. Suwankawin, and S. Sangwongwanich, "Design and implementation of a hybrid output EMI filter for high-frequency common-mode voltage compensation in PWM inverters," *IEEE Trans. Ind. Appl.*, vol. 45, no. 5, pp. 1647–1651, Sep./Oct. 2009.
[25] K. Gulez, A. A. Adam, and H. Pastaci, "Torque ripple and EMI noise minimization in PMSM using active filter topology and field-oriented control," *IEEE Trans. Ind. Electron.*, vol. 55, no. 1, pp. 251–257, Jan. 2008.
[26] D. Hamza, M. Pahlevaninezhad, and P. Jain, "Implementation of a novel digital active EMI technique in a DSP-based dc–dc digital controller used in electric vehicle (EV)," *IEEE Trans. Power Electron.*, vol. 28, no. 7, pp. 3126–3137, Jul. 2013.
[27] K. Borisov, H. L. Ginn II, and A. M. Trzynadlowski, "Attenuation of electromagnetic interference in a shunt active power filter," *IEEE Trans. Power Electron.*, vol. 22, no. 5, pp. 1912–1918, Sep. 2007.
[28] J. Huang and H. Shi, "A hybrid filter for the suppression of common-mode voltage and differential-mode harmonics in three-phase inverters with CPPM," *IEEE Trans. Ind. Electron.*, vol. 62, no. 7, pp. 3991–4000, Jul. 2015.
[29] D. Shin, C. Son, S. Jeon, B. Cho, J. Han, and J. Kim, "A simple low-cost common mode active EMI filter using a push-pull amplifier" in *Proc. 2016 IEEE Energy Convers. Congr. Expo.*, Milwaukee, 2016, pp. 1–5.
[30] D. A. Neamen, *Microelectronics Circuit Analysis and Design*. 3rd ed. New York, NY, USA: McGraw-Hill, 2007.
[31] *International Standard – Methods of Measurement of Touch Current and Protective Conductor Current*, IEC Std. 60990:1999, 1999.
[32] J. Jeong, S. Kim, C. Kim, and J. Kim, "Estimation of the worst-case conducted emission noise due to multiple parallel power converters," in *Proc. 2016 URSI Asia-Pac. Radio Sci. Conf.*, Seoul, 2016, pp. 931–934.
[33] J. Meng, W. Ma, Q. Pan, Z. Zhao, and L. Zhang, "Noise source lumped circuit modeling and identification for power converters," *IEEE Trans. Ind. Electron.*, vol. 53, no. 6, pp. 1853–1861, Dec. 2006.
[34] V. Tarateeraseth, H. Bo, K. Y. See, and F. Canavero, "Accurate extraction of noise source impedance of SMPS under operating condition," *IEEE Trans. Power Electron.*, vol. 25, no. 1, pp. 111–117, Jan. 2010.
[35] *International Standard – Electromagnetic Compatibility (EMC)–Part 4-5: Testing and Measurement Techniques – Surge Immunity Test*, IEC Std. 61000-4-5, 2014.
[36] F. Luo, D. Dong, D. Boroyevich, P. Mattavelli, and S. Wang, "Improving high-frequency performance of an input common mode EMI filter using an impedance-mismatching filter," *IEEE Trans. Power Electron.*, vol. 29, no. 10, pp. 5111–5115, Oct. 2014.

Dongil Shin received the B.S. degree in electronic engineering from Kumoh National Institute of Technology, Gumi, South Korea, in 2012. He is currently working toward the Ph.D. degree in the School of Electrical and Computer Engineering, Ulsan National Institute of Science and Technology, Ulsan, South Korea.

His current research interests include electromagnetic compatibility problems in the power system and the noise reduction techniques.

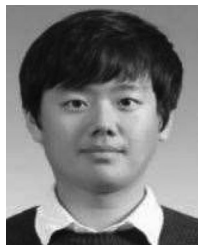

Sangyeong Jeong received the B.S. degree in electrical engineering in 2015 from Ulsan National Institute of Science and Technology, Ulsan, South Korea, where he is currently working toward the Ph.D. degree.

His current research interests include electromagnetic compatibility problems in the power system and the noise reduction techniques.

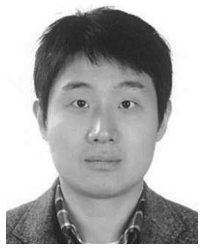

Jingook Kim (M'09–SM'15) received the B.S., M.S., and Ph.D. degrees in electrical engineering from Korea Advanced Institute of Science and Technology, Daejeon, South Korea, in 2000, 2002, and 2006, respectively.

From 2006 to 2008, he was with DRAM design team in Memory Division of Samsung Electronics, Hwasung, South Korea, as a Senior Engineer. From January 2009 to July 2011, he worked in the Electromagnetic Compatibility (EMC) Laboratory, Missouri University of Science and Technology, Rolla, MO, USA, as a Postdoc Fellow. In July 2011, he joined Ulsan National Institute of Science and Technology, Ulsan, South Korea, where he is currently an Associate Professor. His current research interests include high-speed I/O circuits design, 3-D-IC, EMC, electrostatic discharge, RF interference.